Radial Multiscale Cyst Segmentation in Ultrasound Images of Kidney

Abouzar Eslami
Sharif University of Technology
Electrical Eng. Dept.
Tehran, Iran
Email: eslami@mehr.sharif.edu

Shohreh Kasaei
Sharif University of Technology
Computer Eng. Department
Tehran, Iran
Email: skasaei@sharif.edu

Mehran Jahed
Sharif University of Technology
Electrical Eng. Dept.
Tehran, Iran
Email: jahed@sharif.edu

***Abstract*— Cysts are one of the most common lesions in kidneys and can be diagnosed exploiting ultrasound images. In this paper, we develop an automatic approach for cyst segmentation in ultrasound images. The proposed approach comprises three steps: nding a seed point in the object exploiting the Gibbs random eld, detecting the boundary based on multiresolution signal processing and edge re ning, and nally shape model features extracting to verify whether the object is a cyst. The proposed approach is fast and less complex to suit ultrasound exploration applications.**

I. Introduction

The *computer aided diagnosis* (CAD) refers to the usage of computers to help doctors to recognize the abnormal areas in medical images[3]. Although simple renal cysts (uid lled objects) are vaguely mentioned in CAD but they are extremely common in adults and are present in $25-50\%$ of subjects over the age of 50. Approximately, 40% of patients treated by long term hemodialysis develop renal cysts and some kinds of hereditary cysts can affect kidney development [1], [2]. The region growing, snakes, watershed, and texture homogeneity assessment are well known approaches for segmentation and frequently applied to medical images [3], [10]. Since we deal with ultrasound images (which are used in exploration and diagnosis issues), we seek for a fast algorithm therefore iterative approaches listed above become inef cient. In our approach, rst a probability value (exploiting *GRF*) is allocated to each pixel to determine the possibility of being included in a cyst, for each pixel. Indeed a supervised estimation which involves texture and location is performed based on theoretical de nition and training cases of cysts. After extracting the seed point as the point with maximum probability, the image is sliced to radial lines and each line is treated as a $1-D$ sequence, fed to wavelet transform for discontinuity detection in different resolutions (*coarse to ne*). This $1-D$ approach is more computationally ef cient than the $2-D$ multiresolution segmentation techniques. Knowing the edges through all radiuses (slices), the boundary can be constructed by nding their associated points in the image. Object segmentation is accomplished by boundary re nement to suppress unusual deviations in the boundary. To certify doctors and ensure them whether the object is actually a cyst or not, the last section presents shape model parameters. This part gives 3 benchmarks for making decision about object's inherent.

II. Seed Point Extraction

To extract the seed point (a pixel in the object) a probability P_c is allocated to each pixel u of the undergoing image. This probability can tell us how probable it is for pixel u to belong to a cyst. The pixel S associated with the maximum probability will be selected as the seed point.

$$S = \arg\max_u \{P_c(u)\}. \tag{1}$$

Assume that the undergoing image has the size of $p \times q$, therefore **N** (the set of known random variables) is determined by $\mathbf{N} = \{I_1, ..., I_{pq}, L_1, ..., L_{pq}\}$. Where I_k is the intensity of pixel k and L_k is its location. The cystis probability is a function of **N**, de ned by the conditional probability of:

$$P_c(u) = P_u(c \mid \mathbf{N}) = P_u(c \mid \mathbf{N}_u^m). \tag{2}$$

Assuming that the random eld is an *MRF*, the probability can be determined by using just an $m \times m$ neighborhood of u, ($\mathbf{N}_u^m$). This assumption is premised frequently in ultrasound image processing both in segmentation [3] and speckle reduction [4], [5] tasks.

Two empirical principals employed in probability approximation rise from the pathological description of cyst, which de ne it as: *a dark and circular object with usually simple uniform texture* [2], and anatomic kidney characteristics about its dept in ultrasound images. These two principals justify the relation of the cystis probability of each pixel and its intensity, location, and texture [1],[2].

From primary probability theory, choosing maximum of $P(c|\mathbf{N})$ and maximum of $P(c, \mathbf{N})$ are congruent, for an image. Constructing $P(c, \mathbf{N})$, assume that the random variables $\{c, \mathbf{N}\}$ are from *GRF*, their joint probability is in the form of:

$$P(c, \mathbf{N}) = k \exp\left(-U(c, \mathbf{N})\right). \tag{3}$$

$$U(c, \mathbf{N}) = \sum_{V_{c_i}} V_{c_i} \tag{4}$$

where k is a normalizing constant and V_{c_i} is the potential associating with clique c_i (each clique is a subset of random variables). It can be shown that non-negative exponent $U(.)$

guarantees that the Gibbs random field is a Markov process too. More details on *GRF* can be found in [6]. There are three ingredients involved in $U(.)$:

1) position: Existence of skin, fat tissue, and glandular tissue, under probe and the dept of kidney location causes cystis probability to not have a unique distribution for the whole image. Since convex probes are used in image capturing, polar representation of locations (r, θ) is more useful (generally, $r_{min} \leq r \leq r_{max}$ and $|\theta| \leq \theta_l$). The upper and lower limits can vary from one apparatus to another but are identical in different images of one apparatus. Considering the training cases, the following function is proposed as a part of the zero–order clique potential.

$$f(x) = \begin{cases} \frac{4}{5}x^4 & |x| \leq 1 \\ 1 - \exp(-(\ln 5)x^4) & |x| > 1 \end{cases} \tag{5}$$

$$V_1 = f(\tfrac{4}{\pi}\theta) f(\tfrac{r - r_{ave}}{533 - r_{ave}}).$$

2) intensity: This part of the zero–order clique potential rises from the fact that cysts have lower density than normal tissues [2]. Our experimental findings imply that the probability distribution of the cyst's intensity can be discriminated from that of normal tissue's intensity, with acceptable accuracy. Equation (6) determines the role of intensity in the zero–order potential.

$$V_2 = |i_u - (k_1\sigma + \mu)|. \tag{6}$$

Where (μ) and (σ) denote the mean and variance of undergoing image and k_1 is a statistical value, estimated using training data.

3) texture: Here, four different features are extracted to represent texture. Twos of them are the vertical and horizontal lines in a 5×5 neighborhood; and are calculated using $2 - D$ correlation of neighborhood with vertical and horizontal kernels shown in figure 1. Other two features are the expectation value of the difference between the central pixel u and those on the perimeter of two different size windows. Suppose $\mathbf{N}_{W5}$ is the rectangular window of size 5 around u (then $\mathbf{N}_{W5}$ has 25 elements). Also, $\mathbf{N}_{P7}$ and $\mathbf{N}_{P9}$ are the pixels locating on the perimeter of 7×7 and 9×9 rectangular windows, respectively (certainly around u). So $\mathbf{N}_{P7}$ has 24 and $\mathbf{N}_{P9}$, has 32 elements. By this notation following potentials are proposed as higher order potentials:

$$v_3 = |\mathbf{N}_{W5} \star \mathbf{ker}_h - (k_2\sigma + \mu)|. \tag{7}$$

$$v_4 = |\mathbf{N}_{W5} \star \mathbf{ker}_v - (k_3\sigma + \mu)|. \tag{8}$$

$$v_5 = E\{(\mathbf{N}_{P7} - i_u)^2\}. \tag{9}$$

$$v_6 = E\{(\mathbf{N}_{P9} - i_u)^2\}. \tag{10}$$

Where $\star$ denotes the correlation operator. Exploiting these texture features gives the probability map, low–frequency inherent and reduces the spike–like noises in it (notice the large size windows employed). Such characteristic is extremely desirable since we use global maximum of probability and deal with a noisy image (ultrasound images have high amount of noise and speckle, and we just applied a 3 median filter for noise reduction). Totally, the exponent value (4) is constructed by weighting these potential functions. Fig. 2 shows an image and its probability map.

$$U = \sum_{i=1}^{6} W_i V_i. \tag{11}$$

0.1	0.1	1	0.1	0.1
0.1	0.1	1	0.1	0.1
0.1	0.1	1	0.1	0.1
0.1	0.1	1	0.1	0.1
0.1	0.1	1	0.1	0.1

(a)

0.1	0.1	0.1	0.1	0.1
0.1	0.1	0.1	0.1	0.1
1	1	1	1	1
0.1	0.1	0.1	0.1	0.1
0.1	0.1	0.1	0.1	0.1

(b)

Fig. 1. Line detection kernels; (a) vertical $\mathbf{ker}_v$; (b) horizontal $\mathbf{ker}_h$.

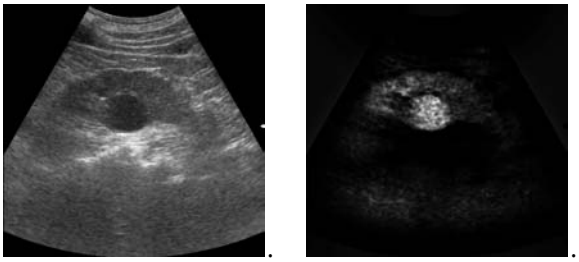

(a) (b)

Fig. 2. (a) Ultrasound image of a kidney cyst; (b) associating cystis probability map.

III. RADIAL SEGMENTATION

Considering the high amount of noise in ultrasound images, here we employ a multiresolution–based decomposition scheme for edge detection (*coarse to fine*). To refrain from two dimensional processing and its computation cost, the object is sliced to some radial segments (number of slices is chosen regarding the objects estimated perimeter) and edge detection through each one of these slices is performed individually. Finally, an edge refinement is applied to improve the overall accuracy of the proposed algorithm. Edge extraction through each segment, independent of adjacent ones, makes the procedure susceptible to noise. To increase its robustness, segmentation is applied to cystis probability (introduced in Section II), instead of the crude image. Since texture information which employs pixel's neighborhood, contributes in the probability calculation, the amount of noise in probability map is less than that in the raw gray–scale image. Also, the exponential function involved in the Gibbs joint probability equation (3), sharpens the edges and increases the contrast between lesion and normal tissue around (compare fig. 2–a and b).

An initial approximation of the lesion perimeter is acquired through four diameters at 0, 45, 90 and 135 degrees. This estimated perimeter determines the number of slices. A big number of slices makes the approach time consuming while a small number yields low angular resolution (which causes probable destructive discontinuity in the boundary). Edges through 8 radii shown in figure 3–a are connected through a first order hold interpolation to construct an enclosed object.

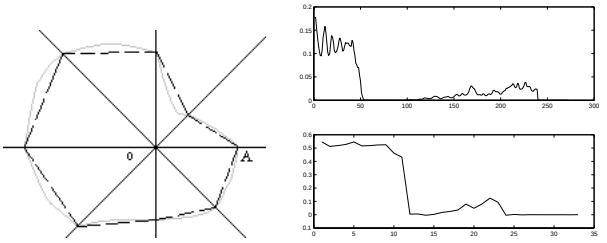

(a) (b)

Fig. 3. (a) The 8 radii of object employed for perimeter estimation; (b) top: a typical sequence of cystis probability on a radius (b) down: associating approximation in level 4.

The number of radial lines will be the same as the perimeter of this arti cial object.

A. multi resolution edge detection

Boundary detection consists of applying an edge detection through each radii, radiated from the seed point. Pixels' cystis probability, among each radius of the object comprise a $1-D$ sequence. Fig. 3-b depicts such a sequence. Regarding the high amount of noise, the sequence is fed to wavelet transform for decomposition in different resolutions.

Let x be a band–limited signal $|f| \leq f_0$. With dyadic wavelet transform, in each level, the frequency space is halved and x is split to two orthogonal subbands (one containing the lower frequency content of x, called the approximation (A), and the other containing the higher half–band of the frequency space called the detail (D)). Down–sampling the two consequent parts by 2, results in half resolution component of input signal [7],[9]. Consequently, after k levels, a coarse approximation with $\frac{1}{2^k}$ resolution is achieved. Explicitly, extraction of discontinuity in such low resolution (containing the least amount of noise), is more reliable than the original data. With a (*coarse to ne* procedure technique, using the information of one level back in the analysis stage, the edge extracted from the low resolution subband can be computed more precisely [10]. Here, the undergoing $x[n]$ is fed to a $4-level$ wavelet analysis tree, with spline biorthogonal wavelet functions of order 6 and 8 [8]. In our approach, symmetry is an essential characteristic for lters, because it makes them linear–phase and prevents dephasing. It is vital to know the amount of delay caused by ltering in each level. Below, signal depicted in Fig. 3–b is the approximation of upper signal in the $\frac{1}{16}$ resolution.

The edge point in CA_4 (wavelet coef cients in level 4), denoted by E_4, is the rst local minimum in the gradient sequence (regarding the sign), which satis es a conditional constraint in gradient amplitude. Local minima of gradient sequence ($\frac{d\,CA}{d\,n}$), correspond to the zero–crossing points in the Laplacian sequence ($\nabla^2\,CA$). so,

$$E_4 = \min_n \begin{cases} \nabla^2[n-\varepsilon]\nabla^2[n+\varepsilon] < 0 \\ \frac{d}{dn}(CA_4[n]) \geq th \end{cases} \tag{12}$$

where th is a fraction of global minimum in gradient. The radius constructing sequence x radiates from the seed point (in the object) to outer part of object. Certainly inner pixels have a bigger cystis probability than outer ones. Consequently, a distinct transition from high–to–low occurs in CA_4 and negative gradients are expected in the transition region, g. 3–b. This justi es equation (12) regarding the sign of the gradient.

Moving one level back to reach a higher resolution (twice), E_i in level i, maps to E_{i-1} in level $i-1$.

$$E_{i-1} = 2 \times E_i - d \tag{13}$$

where d is the delay occurred by ltering in analysis stage. Because of twice resolution, there exists three pixels in the neighborhood of E_{i-1} that can be interpreted as the edge point. Thus, a judgement is inevitable to determine one of these adjacent points as the edge point in this resolution. In fact, CA_{i-1} is used as a benchmark which can either verify E_{i-1} or replace it with one of its two adjacent neighbors, which one has the less value of gradient (respecting to the sign again):

$$\widehat{E}_{i-1} = \min_n(CA_{i-1}[n] - CA_{i-1}[n-1]). \tag{14}$$

$$E_{i-1} - 1 \leq n \leq E_{i-1} + 1. \tag{15}$$

Notice that CA_4 has a far fundamental role in determining the initial edge and CA_3 is just used to re ne it in a short neighborhood. This re nement is iteratively repeated till level one. But moving from level one to level zero does not contain a re nement. Because of high amount of noise in ultrasound images, D_1 is assumed as noise, therefore the nal edge point (E_0, edge in unity resolution) is $\widehat{E}_0 = E_0$ and the last detail is abandoned.

B. boundary re nement

After the edge detection through all radii, a boundary re nement process is applied on the adjacent slices to eliminate the indelicate uctuations in the object boundary. The main idea rises from the shape of the undergoing objects. In fact, with respect to the number of slices, the edge distance in a slice is not allowed to have a value out of the edge distance in its two adjacent slices. Let R_k represent the distance between the edge in the kth slice E_K and the seed point S. Equation (16) imposes such a constraint on the boundary and suppresses undesirable distortions in it.

$$R_k = \|E_k - S\|.$$

$$t = R_k - \tfrac{R_{k-1}+R_{k+1}}{2}.$$

$$\widehat{R}_k = \frac{R_{k-1}+R_{k+1}}{2} + \frac{t \times |R_{k+1} - R_{k-1}|}{2t+\zeta} \tag{16}$$

where $\|.\|$ denotes the Eucledian distance. The proposed lter removes all impulsive uctuations in R, while preserving the steps referring to the smoothing factor ζ. The big values of the smoothing factor reduces the non–linearity characteristic of the lter. Figure 4 shows the object boundary before and after the boundary re nement stage.

(a) (b)

Fig. 4. The effect of boundary re nement. (a)Initial boundary constructed by multiresolution edge detection among different slices; (b)re ned boundary by exerting non–linear lter after 3 iterations.

IV. SHAPE MODEL ASSISTANT

There are some objects with the same texture and intensity as the cysts. It is worth to present a benchmark to assist doctors with diagnosis. Although the objects such as hydronephroses and some imaging artifacts resemble cysts in the texture, but they have different shapes and their shape model presents ef - cient discriminating features. Based on the medical de nition of cysts, these object are usually circular and have a simple shape. Consider $\mathbf{r} = \{r_k\}$ as the set of distances between boundary and center of mass $r_k = \|E_k - C\|$. then:

$$SD = E\{(r - \overline{r})^2\}. \tag{17}$$

$$PSER = \frac{energy\, in\, lower \frac{1}{3}\, of\, PSD}{total\, PSD\, energy}. \tag{18}$$

$$CC = \#\, of\, local\, maxima\, of\, R \tag{19}$$

where C denotes object's center of mass and PSD in feature (18) denotes the power spectral density. The smoothness of **r**, implies the roundness of the object. Three above features give appropriate benchmark of the uniformity of **r**. Before calculating these features a normalization factor $\frac{1}{\max\{r_k\}}$ is applied to **r**. Stochastic information of the addressed features are listed in Table I–B.

V. EXPERIMENTAL RESULTS

Proposed approach is applied to ultrasound images of renal cyst, captured by ESAOTE *technos*^{mp}. Here, 24 healthy cases and 19 patients including females and males aged from 45 to 80, are involved in our experiment. The 17 cases out of these 43 samples are used for training and others for test. Only in 2 cases the seed point was not successfully determined. Successive seed point determining means that the extracted seed point locates in the cyst. Both of failures were caused by some imaging artifacts.

Fig. 5 shows an ultrasound image of a cyst and the result of the proposed segmentation scheme. To present the quantitative results of our automated segmentation process, three different errors are assessed [3]. The *mean of error* (ME) is the mean of the distance between the boundaries de ned by the proposed scheme and those delineated by the radiologist. Also, there are two area error metrics pertaining to the difference of cyst areas in manually delineate and automatic segmentation processe. The *false positive* (FP) volume fraction represents the area determined by the approach while it was not cyst and volume fraction *false negative* (FN) is the cyst area,

TABLE I

(A) BOUNDARY ERRORS CORRESPONDING TO THE APPROACH; (B) STOCHASTIC INFORMATION FOR SHAPE FEATURES.

	ME	FP%	FN%
min	2.88	4.1	15.18
$Ave.$	5.86	11.11	31.25
$Ave\ in$ [3]	6.68	20.85	24.95

(A)

	SD	$PSER$	CC
$Ave.$	11.18	99.97%	2.25
$var.$	54.37	0.0018%	0.5

(B)

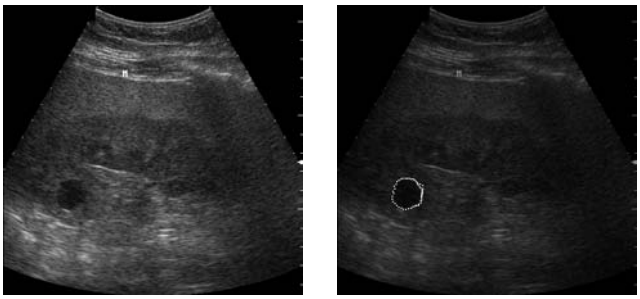

(a) (b)

Fig. 5. Segmentation result; (a)crude image with cyst located in bottom left, (b) segmented cyst by the proposed approach.

omitted in the approach. To acquire normalized criteria *FP* and *FN* are divided by the area of delineated object. The best results are *ME*=2.88, *FP*=4.1%, *FN*=15.18%. Table I–(A) lists the average and minimum of these benchmarks through all 19 cases. The last row of the table represents the average of the benchmarks, resulted from deformable contour–based segmentation applied on breast lesions published in 2003 [3]. By comparison, our proposed scheme is faster and non–iterative while tending to higher accuracy.

ACKNOWLEDGMENT

The rst author would like to thank Mrs. Minoo Naroienejad for her scienti c assistance.

REFERENCES

[1] H. M. Pollack and B. L. McClennan *clinical urigraphy* Second ed. Vol. 2 PP. 1245-1250 W. B saunders company.

[2] D. Sutton, *Text Book of Radiology and Imaging*, Sixth ed. 2003, VOL. 2, PP. 950-952, Churchill Livingstone.

[3] A. Madabhushi and D. N. Mtaxas, *Combining low-,high-level and empirical domain knowledge for automated segmentation of ultrasonic breast lesions*, IEEE transactions on medical imaging, VOL. 22, NO. 2 FEBRUARY 2003.

[4] J. H. Hokland and P. A. Kelly, *Markov Model of Specular and Diffuse Scattering in Restoration of Medical Ultrasound Images*, IEEE transactions on ultrasonics,feroelectrcs and frequency control, VOL. 43, NO. 4 july 1996.

[5] L. Onural, M. Bilge Alp and M. I. Gurelli, *Gibbs random eld model based weight selection for the 2-D adaptive weighted median lter*, IEEE Trans. Pattern Anal. Machine Intell. VOL. 16, NO. 8, Aug. 1994.

[6] S. Geman and D. Geman, *Stochastic Relaxation, Gibbs Distribution and the Baysian Restoration of images*, IEEE Trans. Pattern Anal. Machine Intell. VOL. PMAI-6, NO. 6, Nov. 1984.

[7] I. Daubechies, *Ten lectures on wavelets*, CBMS-NSF conference series in applied mathematics. SIAM Ed, 1992.

[8] A. Cohen, *Ondelettes, analyses multirsolution et traitement numrique du signal*, Ph. D. Thesis, University of Paris IX , DAUPHINE, 1992.

[9] A. N. Akansu and R. A. Haddad *Multiresolution Signal Decomposision, Transforms, Subbands Wavelets*, second ed. 2001, Academic Press.

[10] M. Mignotte, J. Meunier,*A multiscale optimization approach for dynamic contour-based boundary detection issue*, computerized medical imaging and graphics, No. 25, PP. 265-275, 2001, elsevier.